ELSEVIER

Contents lists available at ScienceDirect

Chemical Engineering Science

journal homepage: www.elsevier.com/locate/ces



Engineering enzyme electrode with 3D three-phase interface to boost enzymatic and electrochemical cascade reactions

Siyu Zou^{a,1}, Jie Xiao^{a,b,*}, Xinjian Feng^{a,*}

- a College of Chemistry, Chemical Engineering and Materials Science, Soochow University, Suzhou, Jiangsu Province 215123, PR China
- b School of Chemical and Environmental Engineering, Soochow University, Suzhou, Jiangsu Province 215123, PR China

ARTICLE INFO

Keywords:
Three-phase interface
Enzyme electrode
Enzymatic and electrochemical cascade
reaction
Mathematical modeling
Numerical simulation

ABSTRACT

Enzyme electrodes with two-dimensional three-phase interfaces (2D3PI) have been invented to enhance enzymatic and electrochemical cascade reactions. However, for such interface architecture, the electrode performance is still limited by the intrinsic contradiction between the supply of oxygen (for enzymatic reaction) and the utilization of H_2O_2 (for electrochemical reaction). Herein, we engineered and modelled an electrode featuring a three-dimensional three-phase interface (3D3PI) composed of hollow nanotube arrays with porous walls penetrated into the enzyme layer. This special design allows a drastic increase of the interfacial area for oxygen supply. At the same time, it enhances both H_2O_2 production and utilization, enabling simultaneous intensification of cascade reactions. Results show that optimizing the structure of 3D3PI can improve current generation over 672 times compared to a conventional two-phase interface under investigated conditions.

1. Introduction

Enzyme electrodes based on enzymatic and electrochemical cascade reactions offer advantages like mild reaction conditions, high selectivity, and high reaction efficiency, making them widely used to detect various biomarkers (e.g., glucose (Teymourian et al., 2020), lactate (He et al., 2019), uric acid (Yang et al., 2020), etc.) in the medical field.

Traditionally, the enzyme electrode is constructed at the solid—liquid two-phase interface (2PI for short, Fig. S1a). Oxygen required for the enzymatic reaction can only be supplied from the liquid phase. The low concentration and slow diffusion rate of oxygen in the liquid phase limit the enzyme kinetics, which in turn restricts the linear detection upper limit of the enzyme-based electrochemical sensor. (Lei et al., 2016) To overcome this limitation, we have developed a novel enzyme electrode featuring a solid—liquid—gas three-phase interface (Fig. S1b) (Lei et al., 2016; Mi et al., 2017; Song et al., 2018). This innovative design incorporates a porous hydrophobic substrate that can offer gas transport channels. This enables a rapid supply of high-concentration oxygen from the gas phase directly to the enzymematrix (E-matrix), greatly enhancing enzyme kinetics and electrode performance.

However, previous studies have employed E-matrix deposited as flat

layers on various substrates, including carbon paper (Lei et al., 2016; Song et al., 2018), nanowire arrays (Guan et al., 2019), nanopore arrays (Mi et al., 2017), porous polymer matrices (Wang et al., 2021), and so on. This approach creates a two-dimensional three-phase interface (2D3PI for short, Fig. S1b), limiting both the surface area for oxygen supply and electrochemical reaction. Our previous study (Zou et al., 2023) confirmed that only enzymes near the three-phase interface can get sufficient oxygen, while those further away from the three-phase interface are still in a relatively oxygen-deficient state. This limitation arises from the long diffusion distance of oxygen within the E-matrix and the limited supply area of oxygen. Consequently, oxygen supply and the enzyme kinetics remain limited. Furthermore, our previous study (Zou et al., 2024) has found that only part of the H2O2 produced by the enzymatic reaction can be consumed by the electrochemical reaction, and the rest escapes into the analyte. This observation implies that even if the enzymatic reaction (or H₂O₂ production) is maximized, it does not necessarily mean that the electrochemical reaction (or H₂O₂ utilization) is also maximized. Consequently, achieving a simultaneous optimization of cascade reactions is crucial.

To address these problems, we propose a potential strategy to upgrade the current 2D3PI system to a system with a three-dimensional three-phase interface (3D3PI for short). The 3D3PI penetrates deep

^{*} Corresponding authors.

E-mail addresses: jie.xiao@suda.edu.cn (J. Xiao), xjfeng@suda.edu.cn (X. Feng).

¹ Current address: School of Chemical Engineering, Xiangtan University, Xiangtan, Hunan Province 411105, PR China.

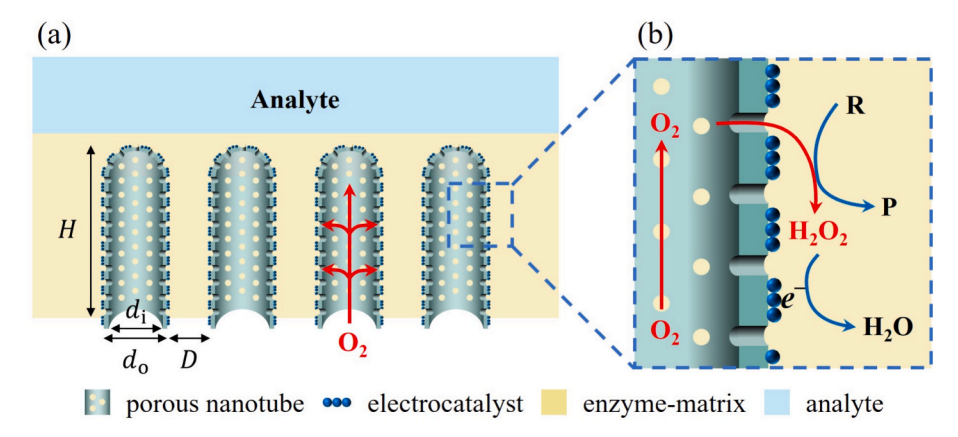


Fig. 1. Schematic diagram of the three-dimensional three-phase interface (3D3PI) for efficient enzymatic and electrochemical cascade reaction. (a) Components of the three-phase interface, in which d_0 , d_i , D, and H represent the outer diameter and inner diameter of the hollow nanotube, the distance between two adjacent nanotubes, and the penetration depth of the nanotube into the enzyme-matrix (E-matrix), respectively. (b) Enlarged view of the three-phase interface, showing the species transport and enzymatic and electrochemical cascade reactions.

into the E-matrix (Fig. 1a), significantly expanding the interfacial area available for both oxygen supply and electrochemical reaction. This enlarged interfacial area becomes a critical prerequisite for achieving efficient cascade reactions and is expected to enhance both the production and utilization of H2O2. Here, we propose a novel 3D3PI constructed using hollow nanotubes with porous walls (Fig. 1a). These porous nanotubes function as gas transport channels, penetrating deep into the E-matrix and offering a substantially larger interfacial area compared to the 2D3PI. The connection between nanotubes and the surrounding air environment ensures a steady and continuous oxygen supply deep into the E-matrix layer. Fig. 1b presents an enlarged view of the three-phase interface, highlighting the efficient oxygen transport and cascade reactions of this design. Oxygen in the air can rapidly diffuse through the pores in the nanotube wall into the E-matrix, providing sufficient oxygen for the enzymatic reaction. The reactant (R), oxygen in the bulk liquid, and oxygen in the bulk gas are diffused into the E-matrix and react with glucose oxidase (GOx) to produce H₂O₂ and other products (P) in situ. One part of the H₂O₂ is consumed on the electrode surface, and the rest escapes into the analyte. The electrons required for the electrochemical reaction are supplied to the electrocatalyst through the nanotube wall. It should be noted that the interfacial structure plays a critical role in governing both mass transfer and cascade reactions within the electrode. Optimizing this interfacial structure to achieve efficient synergies between mass transfer and cascade reactions is the key to developing high-performance electrodes.

Chemical engineering principles, such as theories on fluid mechanics, mass transfer, and reaction engineering, play an important role in the design and optimization of medical devices (e.g., artificial organs (Langer, 2019), bio-membranes (Langer and Peppas, 2024; Peppas and Langer, 2004), and drug delivery systems (Parker et al., 1999; Peppas and Narasimhan, 2014)). These principles have also long been used to understand mass transfer and reaction kinetics within the electrodes in the biomedical field (e.g., glutamate electrodes (Clay and Monbouquette, 2018), cholesterol electrodes (Goyal et al., 2020), and glucose electrodes (Baronas et al., 2021; Bartlett and Pratt, 1993; Gao et al., 2018; Gao and Orazem, 2021; Mell and Maloy, 1975; Parker and Schwartz, 1987)) and other fields (e.g., CO2 electrodes (Bui et al., 2022; Lees et al., 2024)), for ultimately guiding their design. Here, from the perspective of chemical engineering, we present a novel model to capture transport and reaction phenomena for the enzyme electrode featuring a 3D3PI. This innovative design enables significant expansion of the interfacial surface area for both oxygen supply and effective surface area for heterogeneous electrochemical reaction, thereby enhancing the cascade reactions within the electrode. Our model considers both intra-phase and inter-phase mass transport, coupled with the enzymatic and electrochemical cascade reactions. This comprehensive method allows us to explore the effect of the interfacial structure on the electrode performance and reveal the underlying mechanisms. Furthermore, the model facilitates the identification of optimal interfacial structures for maximizing electrode performance. By leveraging these fundamental chemical engineering principles, this work paves the way for the design of next-generation high-performance enzyme electrodes.

2. Model development

2.1. System description and model assumptions

As shown in Fig. 1, the enzyme electrode consists of hollow nanotubes with porous walls, electrocatalyst layers, and an E-matrix. The top part of the outer surface of the nanotube is hydrophilic, and the rest of the nanotube is hydrophobic. The E-matrix and electrocatalyst are immobilized on the hydrophilic surface. The E-matrix is composed of chitosan gel and GOx. The hydrophobic surface of the nanotube forms a gas transport channel. Meanwhile, the nanotube has a hollow bottom surface and a porous sidewall. This structure enables continuous oxygen transfer from the air to the E-matrix. When the electrode is immersed in the analyte, the E-matrix becomes fully wetted by the liquid phase, forming a two-phase layer containing both solid and liquid phases. However, the hydrophobic part of the nanotube remains unwetted, creating internal gas transport channels. Consequently, the solid phase (E-matrix), liquid phase (analyte within the E-matrix), and gas phase (air within the nanotubes) coexist, forming a three-phase interface (Fig. 1a).

This study addresses the challenge of modeling the complex multiscale pore structure of the nanotube, which includes both the nanotubes themselves and the numerous pores on their sidewalls. To overcome this, we make the following assumptions.

- (1) The system is isothermal and at a steady state. The system is modeled at the continuum scale with a two-dimensional computational domain.
- (2) We assume that transport phenomena within each nanotube are identical. This allows us to model a representative sample of nanotubes rather than the entire nanotube population, significantly reducing computational complexity.
- (3) While each nanotube wall contains numerous pores, our previous work (Zou et al., 2023) has demonstrated that optimizing the porous structure can minimize its obstruction to the mass transfer of oxygen from the gas phase to the E-matrix. If the nanotube is properly selected, the efficiency of the oxygen supply through its sidewall can even be comparable to the efficiency when the gas and liquid phases are in

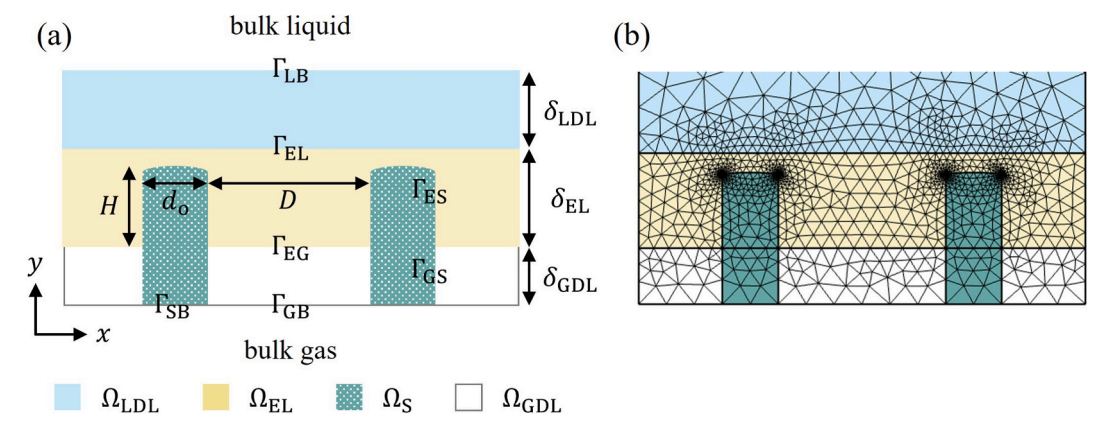


Fig. 2. Schematic diagram of the computational domain and mesh distribution for the 3D3PI enzyme electrode. (a) Computational domain configuration. (b) The mesh distribution. Note that only the local mesh is shown due to significant scale differences between sub-domains, particularly the substantially greater height of Ω_{LDL} relative to other domains.

complete contact. Therefore, instead of explicitly modeling the oxygen diffusion through individual pores on the nanotube sidewall, we employ specific boundary conditions (see the section "Boundary and initial conditions") to account for the overall mass transfer through pores. This simplifies the model without significantly compromising accuracy.

In this study, we developed a model that comprehensively describes the transport phenomena and cascade reactions within the enzyme electrode with a 3D3PI. The electrode is modeled at the continuum scale under the steady-state condition. As shown in Fig. 2a, the computational domain is divided into four sub-domains: the liquid diffusion layer formed by the analyte (LDL, Ω_{LDL}), the E-matrix layer (EL, Ω_{EL}), the hollow nanotube substrate (S, Ω_S), and the gas diffusion layer formed by the air (GDL, Ω_{GDL}). Classified according to the phase states of the species in the computational domain, it can also be divided into two subdomains: the liquid domain ($\Omega_l = \Omega_{LDL} \cup \Omega_{EL}),$ and the gas domain $(\Omega_g = \Omega_S \cup \Omega_{GDL}).$ The mass transfer of H_2O_2 and glucose occurs in the liquid domain (Ω_l), and the mass transfer of oxygen occurs in both liquid and gas domains $(\Omega_l \cup \Omega_g).$ Transfer phenomena outside these regions are considered to have a negligible impact on the system and are not considered. The model incorporates intra-phase and inter-phase mass transfer, homogeneous enzymatic, and heterogeneous electrochemical reactions. The mass transport is described by Fick's law (Bird et al., 2006). The oxygen dissolution from the gas phase to the liquid phase is described by Henry's law (Sander, 2015). The enzymatic reaction is modeled by the ping-pong mechanism (Tao et al., 2009). The current generation is calculated based on Faraday's and Fick's laws (Bard et al., 2022; Baronas et al., 2021).

2.2. Governing equations

In the Ω_{GDL} , since only oxygen participates in the enzymatic reaction, the mass transfer of other species in the gas phase is not considered. The governing equation can be written as,

$$-D_{\text{GDL},O_2} \nabla^2 [O_2]_g = 0 \tag{1}$$

where D_{GDL,O_2} is the effective diffusion coefficient of oxygen in the GDL, $m^2 s^{-1}$; $[O_2]_g$ is the concentration of oxygen in the gas phase, mol m⁻³.

Inside the Ω_S , like the Ω_{GDL} , only the mass transfer of oxygen is considered. The governing equation can be written as,

$$-D_{S,O_2} \nabla^2 [O_2]_g = 0 (2)$$

where D_{S,O_2} is the effective diffusion coefficient of oxygen in the nanotube, $m^2 s^{-1}$.

To simulate the mass transfer of oxygen in the gas transport channel with characteristic lengths that are smaller than the mean free path of

oxygen, the Knudsen diffusion (Bird et al., 2006) must be considered in the model. The effective diffusion coefficient of oxygen (D_{GDL,O_2} or D_{S,O_2}) is calculated via the Wilke-Bosanquet model (Chen et al., 2013),

$$\frac{1}{D_{\text{GDL,O}_2}}$$
 or $\frac{1}{D_{\text{S,O}_2}} = \frac{1}{D_{\text{O}_2}} + \frac{1}{D_{Kn,O_2}}$ (3)

where D_{O_2} is the molecular diffusion coefficient of oxygen in a free environment, $m^2 s^{-1}$, which is calculated by an empirical correlation (Poling et al., 2001); D_{Kn,O_2} is the Knudsen diffusion coefficient of oxygen in the gas channel, $m^2 s^{-1}$, which can be calculated based on the kinetics theory (Poling et al., 2001),

$$D_{Kn,O_2} = \frac{L}{3} \sqrt{\frac{8RT}{\pi M_{O_2}}} \tag{4}$$

where L is the characteristic length of the gas channel, m, $L = d_i$ in the S, L = D in the GDL; R is the ideal gas constant, 8.314 J mol⁻¹ K⁻¹; T is system temperature, K; $M_{\rm O_2}$ is the molecular weight of oxygen, 0.032 kg mol⁻¹.

In the Ω_{EL} , the governing equation can be written as,

$$-D_{\mathrm{EL},i}\nabla^{2}[i]_{1} = R_{i} \tag{5}$$

where $D_{\text{EL},i}$ is the diffusion coefficient of species i in the EL, $\text{m}^2 \, \text{s}^{-1}$; $[i]_1$ is the concentration of species i in the liquid phase, mol m^{-3} ; R_i is the homogeneous enzymatic reaction rate of species i, $\text{mol m}^{-3} \, \text{s}^{-1}$. The symbol i denotes three species, i.e., glucose, oxygen, and H_2O_2 . The enzymatic kinetics is modeled as the ping-pong mechanism (Tao et al., 2009), which consists of two sequential reaction steps,

$$E_O + G \xrightarrow{k_1} E_R P \xrightarrow{k_2} E_R + P \tag{6}$$

$$E_R + O_2 \xrightarrow{k_3} E_O(H_2O_2) \xrightarrow{k_4} E_O + H_2O_2$$
 (7)

where E_O is the oxidized form of GOx; E_R is the reduced form of GOx; G is the glucose; P is the by-product glucono- δ -lactone; E_RP and $E_O(H_2O_2)$ are two enzyme-product complexes; k_1 , k_2 , k_3 , and k_4 are kinetics constants. It is assumed that the enzymatic reaction reaches a steady state rapidly. The reaction rate of species i can be expressed as (Parker and Schwartz, 1987),

$$R_{i} = \pm \frac{\alpha[E_{T}]}{\frac{\beta_{G}}{|G|_{1}} + \frac{\beta_{O_{2}}}{|O_{2}|_{1}} + 1}$$
(8)

where $\alpha = \frac{k_2 k_4}{k_2 + k_4}$; $\beta_G = \frac{k_2 k_4}{k_1 (k_2 + k_4)}$; $\beta_{O_2} = \frac{k_2 k_4}{k_3 (k_2 + k_4)}$; $[E_T]$ is the total concentration of the active enzyme, mol m^{-3} ; $[G]_1$ is the concentration of

glucose in the liquid phase; $[O_2]_1$ is the concentration of oxygen in the liquid phase. It is assumed that all glucose oxidases are active and uniformly distributed in the EL. The positive value of the R_i represents the production rate of H_2O_2 , and the negative value represents the consumption rate of glucose or oxygen.

In the Ω_{LDL} , the governing equation can be written as,

$$-D_{\text{LDL},i}\nabla^2[i]_1 = 0 \tag{9}$$

where $D_{\text{LDL},i}$ is the diffusion coefficient of species i in the LDL, $\text{m}^2 \, \text{s}^{-1}$; The symbol i also denotes three species, i.e., glucose, oxygen, and H_2O_2 .

All model parameters are listed in Table S1 (see Supporting Information).

2.3. Boundary and initial conditions

The boundary indicators are also displayed in the Fig. 2a, where Γ_{LB} is the interface between the LDL and the bulk liquid, Γ_{EL} is the interface between the EL and LDL, Γ_{EG} is the interface between the EL and the GDL, Γ_{GB} is the interface between the GDL and the bulk gas, Γ_{SB} is the interface between the hollow nanotube substrate and the bulk gas, Γ_{ES} is the interface between the EL and the substrate, Γ_{GS} is the interface between the GDL and the hollow nanotube substrate.

At the Γ_{LB} , the concentration of every species is almost equal to the concentration of the corresponding species in the bulk solution. (Baronas et al., 2021) The fixed-value boundary conditions are applied,

$$\begin{cases} [G]_{l} = [G]_{l,b} \\ [O_{2}]_{l} = [O_{2}]_{l,b} = H_{O_{2}}^{qp} P_{O_{2}} \\ [H_{2}O_{2}]_{l} = [H_{2}O_{2}]_{l,b} = 0 \end{cases}$$
(10)

where $[G]_{1,b}$, $[H_2O_2]_{1,b}$, and $[O_2]_{1,b}$ are the concentration of glucose, H_2O_2 , and oxygen in liquid bulk, respectively, they are assumed to remain constant. The glucose concentration in the liquid bulk is 1000 mM in the current study. The H_2O_2 concentration in the liquid bulk is set as 0 because its production is very low, and initially there is no H_2O_2 in the bulk solution. The oxygen concentration in the liquid bulk is equal to the dissolved oxygen concentration in an aqueous solution. It is calculated by Henry's law, where $H_{O_2}^{\mathcal{O}}$ is Henry's law solubility constant of oxygen in the air–water system, which is defined via equilibrium concentration in the liquid phase and the equilibrium pressure in the gas phase, mol m⁻³ Pa⁻¹; P_{O_2} is the partial pressure of oxygen in the air at 20°C, which can be calculated by Dalton's law of partial pressures,

$$P_{O_2} = P_{env} X_{O_2} (11)$$

where $P_{\rm env}$ is the environment pressure, which is set as 101.3 kPa; $X_{\rm O_2}$ is the molar volume of oxygen in the air, which is set as 21%.

At Γ_{EL} , the flux of each species through the interface is set to be equal to the outgoing one. The matching condition is applied,

$$-D_{\mathrm{EL},i}\nabla[i]_{\mathrm{l}} = -D_{\mathrm{LDL},i}\nabla[i]_{\mathrm{l}} \tag{12}$$

where $[i]_1$ is the concentration of species i in the liquid domain.

At Γ_{EG} , the oxygen must be transported through the three-phase interface and dissolved in the liquid before the enzymatic reactions take place. It has continuity of the mass flux across the boundary, but the concentration profile on both sides is discontinuous. (Geankopolis, 1993) Henry's law (Sander, 2015) is used to describe the dissolution equilibrium between the gas phase and the liquid phase. The dissolved oxygen concentration in the liquid phase is calculated by,

$$[O_2]_1 = H_{O_2}^{cp} p_{O_2} \tag{13}$$

where p_{0_2} is the partial pressure of oxygen in the air, Pa, it is related to the local oxygen concentration and temperature.

The air is assumed to obey the ideal gas law. Hence, the oxygen

concentration in the gas phase can be calculated based on the partial pressure of oxygen and the gas temperature,

$$[O_2]_g = \frac{p_{O_2}}{RT} \tag{14}$$

where R is the ideal gas constant, $8.314 \, \mathrm{J} \, \mathrm{mol}^{-1} \, \mathrm{K}^{-1}$; T is temperature, K. Combining equations (13) and (14), it can be found that the oxygen concentration in the gas phase and the dissolved oxygen concentration in the liquid phase are subject to an equilibrium relationship (see equation (15). This relationship is also known as the partition condition. (Geankopolis, 1993) The $K_{O_2} = H_{O_2}^{\varphi}RT$ is the partition coefficient between two phases. In the air–water system, $K_{O_2} \ll 1$, it implies the $[O_2]_1 \ll [O_2]_g$. The partition condition is written as,

$$\frac{[O_2]_1}{[O_2]_g} = H_{O_2}^{cp}RT \tag{15}$$

The dissolved flux of oxygen through the GDL is equal to the corresponding absorbed flux entering the EL. The matching condition is applied,

$$-D_{\text{GDL},O_2}\nabla[O_2]_{\sigma} = -D_{\text{EL},O_2}\nabla[O_2]_{1}$$

$$\tag{16}$$

The boundary conditions in equations (15) and (16) enforce the concentration discontinuity condition and maintain flux continuity at the interface between GDL and EL.

At Γ_{EG} , there is no mass transfer for glucose and H_2O_2 . The zero-flux boundary conditions are applied,

$$\begin{cases}
-\boldsymbol{n} \cdot \left(-D_{\text{EL},G} \nabla[G]_{1} \right) = 0 \\
-\boldsymbol{n} \cdot \left(-D_{\text{EL},H_{2}O_{2}} \nabla[H_{2}O_{2}]_{1} \right) = 0
\end{cases}$$
(17)

where n denotes the outward pointing normal of the boundary.

At Γ_{GS} , the oxygen flux exchanged between the Ω_S and Ω_{GDL} is equal. The matching condition is applied,

$$-D_{GDL,O_2}\nabla[O_2]_{g} = -D_{S,O_2}\nabla[O_2]_{g}$$
(18)

At Γ_{GB} and Γ_{SB} , the oxygen concentration is equal to the oxygen concentration in the bulk gas. The fixed value boundary condition is applied,

$$[O_2]_g = [O_2]_{g,b} \tag{19}$$

where $[O_2]_{g,b}$ is the oxygen concentration in gas bulk, which is assumed to remain constant

At Γ_{ES} , for oxygen, it is assumed that the oxygen supply efficiency of the pores on the nanotube wall is comparable to the efficiency when the gas and liquid phases are in complete contact. Therefore, the boundary conditions here are the same as those at Γ_{EG} ,

$$\frac{[O_2]_1}{[O_2]_g} = H_{O_2}^{op} RT \tag{20}$$

$$-D_{S,O_2}\nabla[O_2]_{g} = -D_{EL,O_2}\nabla[O_2]_{l}$$
(21)

At Γ_{ES} , there is no mass transfer for glucose. The zero-flux boundary condition is applied,

$$-\boldsymbol{n}\cdot\left(-D_{\mathrm{EL},G}\nabla[G]_{1}\right)=0\tag{22}$$

At Γ_{ES} , the H_2O_2 produced by the enzymatic reaction is reduced by the action of the electrocatalyst, and the reduction current is generated at the same time. The mechanism of electrochemical reduction of H_2O_2 is,

$$H_2O_2 + 2e^- + 2H^+ \rightarrow 2H_2O$$
 (23)

where e^- is transported by the nanotube wall (Fig. 1b); ${\rm H^+}$ is provided by the analyte.

When electrochemical reactions are considered, the H₂O₂ will be

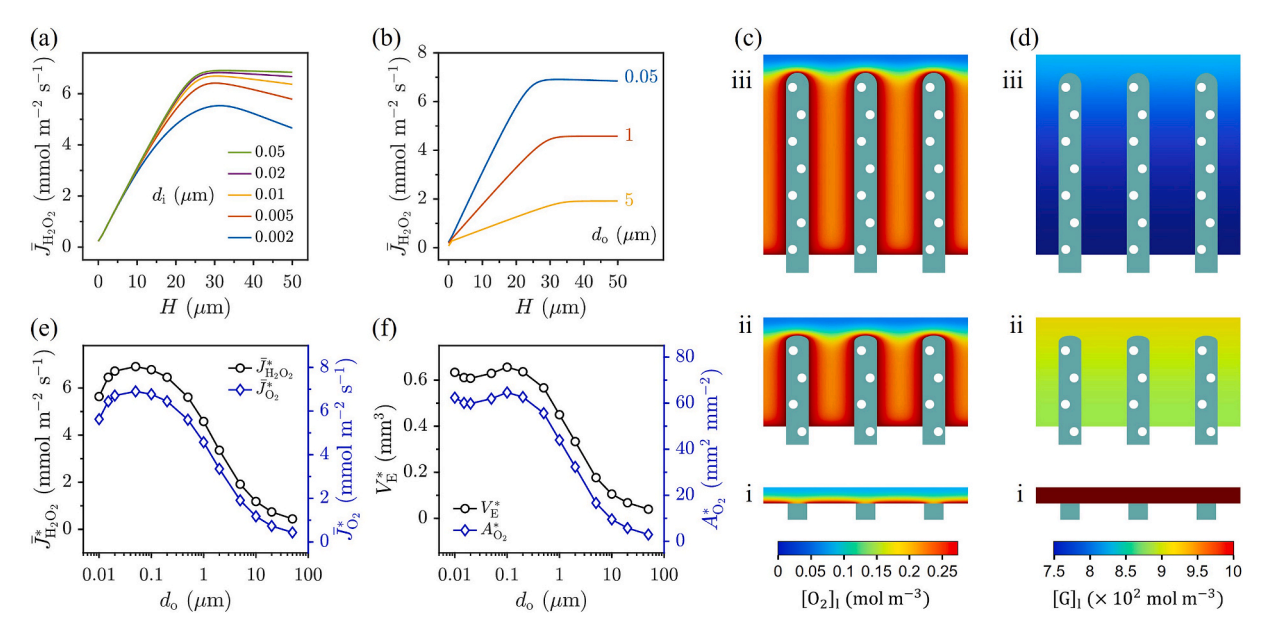


Fig. 3. Effect of the inner diameter (d_i) and outer diameter (d_0) of the hollow nanotube, and the penetration depth (H) of the nanotube into the E-matrix on enzymatic reaction in the electrode with 3D3PI, where the distance between two adjacent nanotubes is D=1000 nm. (a) shows the production rate of H_2O_2 $(\overline{J}_{H_2O_2})$ under different H and d_i , where $d_0=0.05$ μ m. (b) shows $\overline{J}_{H_2O_2}$ under different H and d_0 . (c) and (d) show the oxygen concentration $([O_2]_I)$ and the glucose concentration $([G]_I)$ within the E-matrix, respectively, where i illustrates 2D3PI, ii and iii are for 3D3PI. (e) shows maximum production rate of H_2O_2 $(\overline{J}_{H_2O_2}^*)$ and maximum supply rate of oxygen $(\overline{J}_{O_2}^*)$ as a function of d_0 when $\overline{J}_{H_2O_2}$ reaches maximum.

consumed under the electrochemical reaction. The electrode surface is imposed with specific boundary conditions to simulate the heterogeneous electrochemical reaction. In the experiment, the electrochemical reaction rate can reach a peak value by adjusting the experimental parameters (e.g., the overpotential, the amount of electrocatalyst). Hence, for a diffusion-controlled process, the $\rm H_2O_2$ concentration on the electrode surface is assumed to be zero. The fixed-value boundary condition is applied,

$$[H_2O_2]_1 = 0 (24)$$

where $[H_2O_2]_1$ is the concentration of H_2O_2 in the liquid phase close to the electrode surface, mol m⁻³.

The current density on the electrode surface depends upon the normal H_2O_2 flux across the electrode surface,

$$j = nF \cdot (\mathbf{n} \cdot \mathbf{J}_{H_2O_2}) \tag{25}$$

where j is the current density, A m⁻²; n is the stoichiometric number of electrons for an electrochemical reaction, n=2; F is the Faraday constant, 96485 C mol⁻¹; $n \cdot J_{\rm H_2O_2}$ is the H₂O₂ normal flux caused by the electrochemical reaction on the electrode surface, mol m⁻² s⁻¹.

The current generation is related to the mean current density and the apparent area of the electrode,

$$i = \bar{j}A_{\rm e} \tag{26}$$

where *i* is the current generation, A; \bar{j} is the mean current density, A m⁻², its definition can be found in the Supporting Information; A_e is the apparent area of the electrode, m². In the current study, $A_e = 0.2$ cm².

At Γ_{ES} , when electrochemical reactions are not considered, there is no mass transfer for H_2O_2 . The zero-flux boundary condition is applied,

$$-\boldsymbol{n}\cdot\left(-D_{\mathrm{EL},\mathrm{H}_{2}\mathrm{O}_{2}}\nabla[\mathrm{H}_{2}\mathrm{O}_{2}]_{\mathrm{I}}\right)=0\tag{27}$$

All other boundaries are applied with zero-flux boundary conditions for each species, which means no mass transfer across these boundaries,

$$-\mathbf{n}\cdot(-D_i\nabla[i])=0\tag{28}$$

where D_i and [i] are the diffusion coefficient and concentration of each species, respectively.

At the initial state, the glucose concentration in the liquid phase $([G]_{l,0})$ is equal to the glucose concentration in the bulk solution. The oxygen concentration in the liquid phase $([O_2]_{l,0})$ is equal to the initial dissolved oxygen concentration in the bulk solution. The H_2O_2 concentration in the liquid phase $([H_2O_2]_{l,0})$ is equal to 0, which represents no H_2O_2 in the system in the initial condition. The oxygen concentration in the gas phase $([O_2]_{g,0})$ is equal to the oxygen concentration in the bulk gas.

$$\begin{cases}
[G]_{l,0} = [G]_{l,b} \\
[O_2]_{l,0} = [O_2]_{l,b} = H_{O_2}^{op} P_{O_2} \\
[H_2O_2]_{l,0} = 0 \\
[O_2]_{g,0} = [O_2]_{g,b} = \frac{P_{O_2}}{RT}
\end{cases} (29)$$

2.4. Numerical implementation

All governing equations were solved at steady state using COMSOL Multiphysics. These numerical procedures were realized using the finite element method. The relative tolerance of the solver was set as 0.001. The free triangular meshes are applied to the whole computational domain. Fine meshes are applied inside Ω_{EL} and on Γ_{EG} and Γ_{ES} to capture sharp gradients of physical quantities caused by enzymatic and electrochemical reactions. A typical mesh is shown in Fig. 2b.

After solving the governing equations, the species concentration, reaction rate, species flux, and other information can be obtained and analyzed. Quantificational analysis methods are provided in the Supporting Information.

3. Results and discussion

3.1. Enhanced enzymatic reaction with 3D3PI

In this study, a matrix of nanotubes with porous walls was used as oxygen transport channels. When oxygen diffusion occurs inside the nanotube, the diffusion flux of oxygen is possibly reduced by the collisions between oxygen molecules and the walls. Therefore, the inner diameter of the nanotube significantly affects the oxygen diffusion inside it. If the inner diameter is significantly smaller than the mean free path of oxygen molecules, molecule-wall collisions will occur more frequently than molecule-molecule collisions. This diffusion mechanism is known as the Knudsen diffusion. As the inner diameter increases, the probability of molecule-molecule collisions and molecule-wall collisions are comparable. The diffusion mechanism is dominated by both Knudsen diffusion and molecular diffusion. The molecular collisions dominate until the inner diameter is large enough. The diffusion mechanism becomes free molecular diffusion. Since a large variation in the inner diameter can cause the diffusion mechanism to shift from free diffusion to Knudsen diffusion, ultimately reducing the oxygen supply, it is necessary to explore the effect of the inner diameter of hollow nanotubes on the enzymatic reaction first.

To investigate the status of the enzymatic reaction, we evaluated the production rate of $\rm H_2O_2$. Fig. 3a shows the relationship between the production rate of $\rm H_2O_2$ and the penetration depth of the nanotube into the E-matrix and compares the production rate of $\rm H_2O_2$ under different inner diameters of nanotubes. Here, the outer diameter of the nanotube (d_o) is fixed at $0.05~\mu m$. The inner diameter of the nanotube (d_i) is varied but remains less than or equal to the outer diameter. Notably, the case of $d_i=d_o$ represents an ideal situation where the nanotube wall is absent and the gas phase is in direct contact with the E-matrix. The results reveal a general downward trend in the production rate as the inner diameter decreases. This can be primarily attributed to the reduced diffusivity of oxygen within the smaller inner diameter (see Fig. S2), which hinders the oxygen supply and finally limits the enzymatic reaction.

Beyond the inner diameter, the penetration depth of the nanotube into the E-matrix also plays a crucial role in the oxygen supply. As can be seen from Fig. 3a, increasing the penetration depth significantly increases the production rate of H₂O₂. This can be attributed to the enhanced oxygen supply facilitated by the larger interfacial area at the 3D3PI. However, as the penetration depth increases, the diffusion distance of oxygen from the bulk gas deep into the E-matrix grows. When the penetration depth reaches a critical value (i.e., about 30 µm in Fig. 3a), this may lead to reduced oxygen availability within the nanotube, particularly in regions far from the bulk gas. However, the influence of penetration depth on gas transport depends on the inner diameter of the nanotubes. When the inner diameter is large (e.g., d_i 0.02 μm), the diffusivity of oxygen remains sufficiently large (Fig. S2). Consequently, even with increasing penetration depth, oxygen can still be effectively supplied throughout the nanotube from bulk gas. Therefore, there is no significant drop in the production rate of H₂O₂ (Fig. 3a) with further increasing penetration depth. In contrast, once the inner diameter is restricted (e.g., $d_{\rm i}=0.002\,\mu\text{m}$), the diffusivity of oxygen becomes significantly limited (Fig. S2). This leads to a severe shortage of oxygen supply throughout the nanotube, especially in the part of the nanotube far from the bulk gas. As a result, the production rate of H₂O₂ shows a significant decrease (Fig. 3a) with a further increase in the penetration depth. This phenomenon becomes more pronounced with even deeper penetration depth.

Our analysis reveals that both the inner diameter and the penetration depth are crucial for the oxygen supply within the 3D3PI, ultimately influencing $\rm H_2O_2$ production. To achieve optimal performance for the enzymatic reaction, the inner diameter should be made as large as possible to minimize the oxygen diffusion limitation. In other words, thinner nanotube walls are preferable. Moreover, there exists an optimal

penetration depth beyond which the oxygen supply becomes limited. We will identify its optimal value in the following content.

Given the significant oxygen supply limitation imposed by small inner diameters, they need not be considered in maximizing enzymatic reactions. To this end, we make the following assumptions in the following contents. Firstly, we assume that the thickness of the nanotube wall can be neglected. In this case, the inner diameter equals the outer diameter, and they change together. Secondly, we only study the case of large outer diameter ($d_0 \ge 0.05 \,\mu\text{m}$), which ensures that the oxygen supply is no longer limited by the nanotube diameter. Based on the above assumptions, the influence of the outer diameter of the nanotube is discussed next. As shown in Fig. 3b, regardless of the outer diameter, the production rate of H2O2 continues to increase with the increase of penetration depth until a critical depth is reached. At shallow penetration depths (e.g., $H < 30 \mu m$), the production rate exhibits an almost linear relationship with the penetration depth. This is mainly because increasing the penetration depth can expand the supply area of oxygen, thereby enhancing the oxygen supply. Overall, these results highlight the significant advantage of 3D3PI in enhancing enzymatic reactions. Nevertheless, it is important to note that endlessly increasing the penetration depth does not translate to a limitless increase in H₂O₂ production. When the penetration depth is beyond a certain value, the production rate of H₂O₂ reaches a plateau. We will examine the underlying causes of the above phenomenon in the following contents.

The previous study (Zou et al., 2023) confirms that the H₂O₂ production is primarily determined by the oxygen supply. We first plotted the oxygen concentration in the E-matrix to visualize the mass transfer of oxygen in the E-matrix (Fig. 3c). In the 2D3PI (Fig. 3c-i), the E-matrix far from the three-phase interface exhibits a significant lack of oxygen. This contrasts sharply with the 3D3PI (Fig. 3c-ii and iii), where most of the E-matrix maintains high oxygen concentration. This is the core reason for the increased H2O2 production as the penetration depth increases. Nevertheless, the enzyme kinetics (equation (8) depends on the concentrations of two enzymatic substrates (oxygen and glucose). Therefore, the glucose supply also plays an important role in determining H₂O₂ production. It should be noted that the glucose supply completely overdosed in the previous study (Zou et al., 2023; Zou et al., 2024). The oxygen supply at the 2D3PI is also insufficient to completely consume the supplied glucose. Compared with the 2D3PI, the 3D3PI offers a much larger supply area of oxygen. The oxygen supply in the 3D3PI is improved by several orders of magnitude (Fig. S3), and the glucose supply becomes a factor that must be considered. To explore the reasons behind the eventual plateauing of H₂O₂ production, we next analyzed the mass transfer of glucose in the E-matrix (Fig. 3d). As the penetration depth increases (Fig. 3d-ii and iii), both the mean diffusion distance and time required for glucose to diffuse from bulk liquid into the E-matrix also increase, which impedes the mass transfer of glucose deep into the E-matrix. This can be demonstrated in Fig. 3d-ii and iii, as the nanotubes penetrate deeper, the glucose concentration in the Ematrix away from the bulk liquid progressively decreases. This implies that the glucose supply within the E-matrix becomes insufficient as the penetration depth increases, thereby limiting enzyme kinetics and H₂O₂ production. In other words, a deep penetration depth of the nanotube into the E-matrix facilitates the mass transfer of oxygen but impedes the mass transfer of glucose. The interplay between these two factors leads to the H₂O₂ production to initially rise with increasing nanotube height and then eventually stabilize.

Fig. 3e shows the maximum production rate of $\rm H_2O_2$ as a function of the outer diameter of the nanotube. When the outer diameter is small (e. g., $d_o \leq 0.05~\mu m$), the maximum production rate exhibits an increasing trend as the diameter increases. A small outer diameter necessarily leads to a small inner diameter, thus limiting the diffusivity of oxygen (Fig. S2) inside the nanotube and the oxygen supply (Fig. 3e). Given the previous assumptions, increasing the outer diameter can also increase the inner diameter, and alleviate the oxygen diffusion limitations (Fig. 3e), ultimately increasing the $\rm H_2O_2$ production. However, when the outer

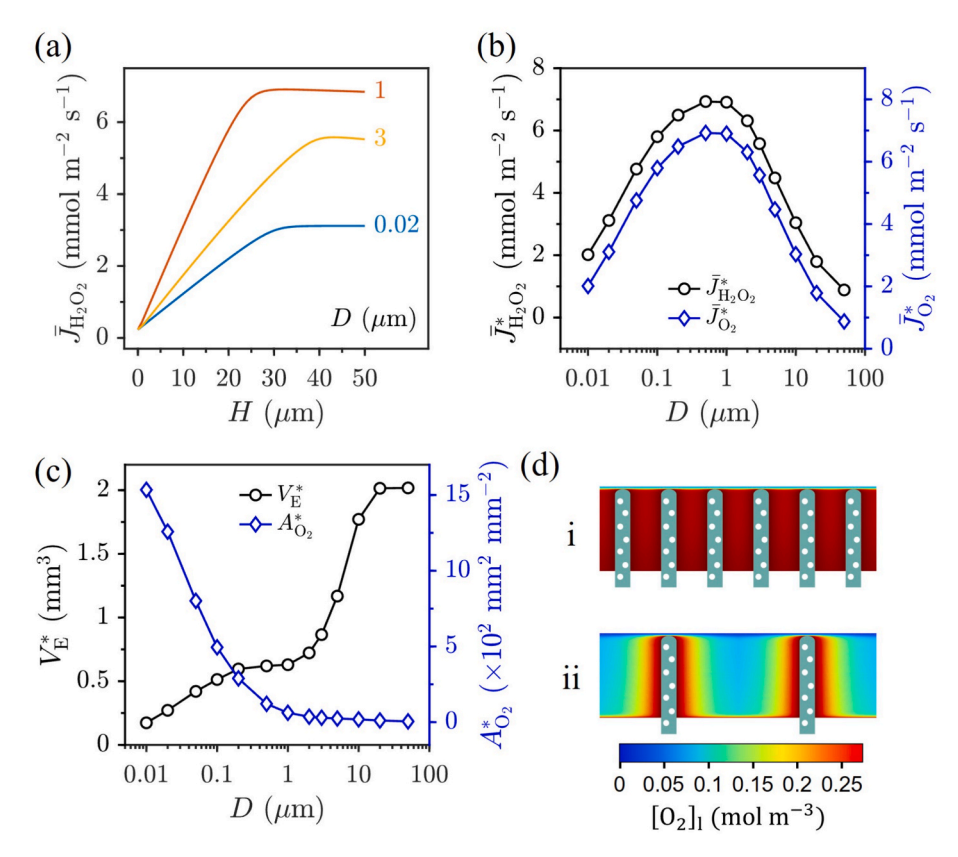


Fig. 4. Effect of the distance between two adjacent nanotubes (*D*) and *H* on the enzymatic reaction in the electrode with 3D3PI, where $d_0 = 0.05 \,\mu\text{m}$. (a) shows the $\overline{J}_{\text{H}_2\text{O}_2}$ under different *H* and *D*. (b) shows the $\overline{J}_{\text{H}_2\text{O}_2}^*$ as a function of *D*. (c) shows V_{E}^* and $A_{\text{O}_2}^*$ as a function of *D* when $\overline{J}_{\text{H}_2\text{O}_2}$ reaches maximum. (d) shows $[\text{O}_2]_1$ within the E-matrix.

diameter is large (e.g., $d_0 > 0.05~\mu m$), the maximum production rate of H_2O_2 shows a continuous decreasing trend when the outer diameter is increased. This can be explained from two perspectives. On the one hand, the enzyme amount between nanotubes decreases with the increase of outer diameter (Fig. 3f). On the other hand, when the distance between two adjacent nanotubes remains unchanged, increasing the outer diameter reduces the number density of nanotubes within the Ematrix, thereby reducing the supply area of oxygen (Fig. 3f) and the supply rate of oxygen (Fig. 3e). Consequently, the combined effect of these factors leads to a continuous decrease in the maximum production rate of H_2O_2 .

Our findings demonstrate a significant improvement in $\rm H_2O_2$ production when employing a 3D3PI compared to the 2D3PI. Taking $d_{\rm o}=0.05~\mu m$ as an example, the 3D3PI achieves a maximum $\rm H_2O_2$ production that is approximately 30 times higher than the 2D3PI. This enhancement is even higher under conditions of sufficient supply of enzymatic substrates (oxygen and glucose). These results prove that the 3D3PI offers a superior strategy for enhancing enzymatic reactions compared to the traditional 2D3PI.

In addition to the inner diameter and outer diameter of the hollow nanotube and the penetration depth of the nanotube into the E-matrix, the distance between two adjacent nanotubes is also an important parameter affecting the interfacial structure. To identify the optimal structure for the enzymatic reaction, we further evaluated the effect of the distance on the enzymatic reaction.

As shown in Fig. 4a, unlike the effect of nanotube diameter, the effect of the distance between two adjacent nanotubes on the $\rm H_2O_2$ production is more complex. It can be found that when the distance is too wide (e.g., $D=3~\mu m)$ or too narrow (e.g., $D=0.02~\mu m)$, the maximum $\rm H_2O_2$ production is limited. The $\rm H_2O_2$ production can only reach a relatively high level when the distance is at a medium value (e.g., $D=1~\mu m)$.

Fig. 4b provides a clear visualization of how the $\rm H_2O_2$ production changes with the distance. The maximum production rate of $\rm H_2O_2$ exhibits a non-monotonic trend, initially increasing and then decreasing with the distance. Notably, Fig. 4b suggests that the oxygen supply directly determines this trend. This is consistent with the conclusion of our previous study (Zou et al., 2023).

The distance affects the enzyme amount on the one hand and the supply area of oxygen on the other hand. When nanotubes are densely arranged (e.g., $D \leq 1~\mu m$), even if the supply area of oxygen is quite abundant (Fig. 4c), there is insufficient enzyme between nanotubes (Fig. 4c). This limits the capacity of the E-matrix to consume oxygen. As shown in Fig. 4d-i, the oxygen accumulates within the E-matrix and maintains a high concentration level. In this case, the gradient of oxygen concentration is too small to maintain the supply rate of oxygen at a high level.

As the distance increases (Fig. 4c), the amount of enzyme between nanotubes grows, enhancing the capacity of the E-matrix to consume oxygen. This results in an increase in the gradient of oxygen concentration, driving an increase in the supply rate of oxygen (Fig. 4b, the supply rate of oxygen is greatly increased when D increases from 0.01 to 1 μ m).

When the distance between two adjacent nanotubes reaches the point at which they are sparsely arranged (e.g., $D=10~\mu m$), the number density of nanotubes decreases dramatically. This greatly reduces the supply area of oxygen (Fig. 4c). On the other hand, it significantly increases the mean diffusion distance and time of oxygen within the Ematrix, impeding the mass transfer of oxygen. The low oxygen concentration in the E-matrix confirms this limitation (Fig. 4d-ii). Consequently, the supply rate of oxygen decreases.

In summary, only when nanotubes are arranged at a moderate distance (e.g., $D=1~\mu m$), the balance between sufficient enzyme amount

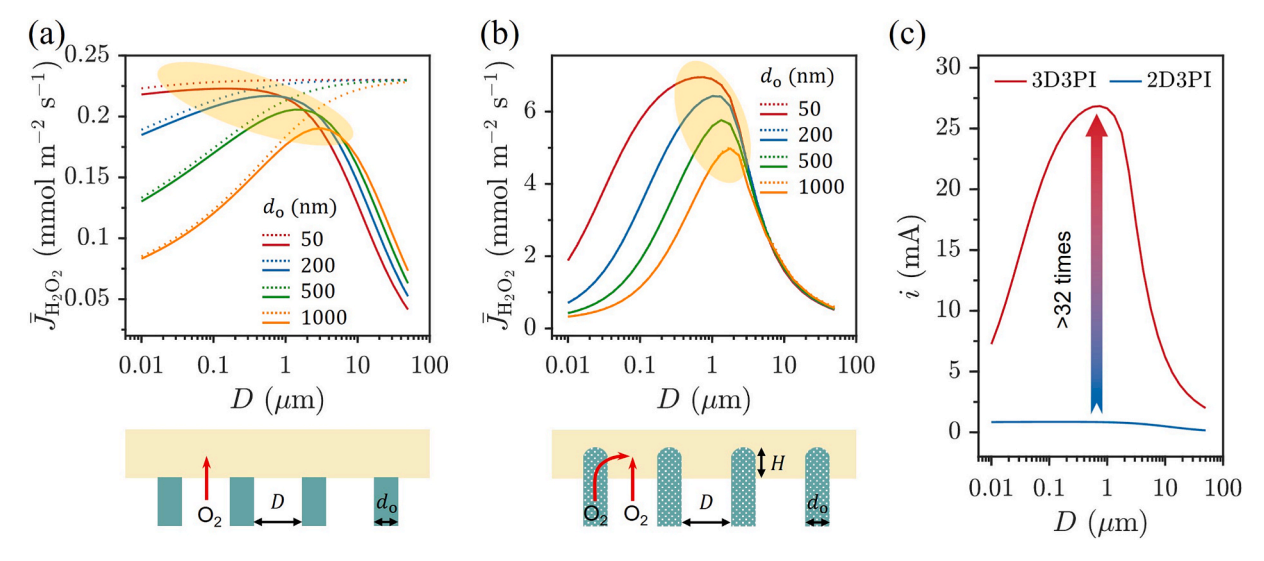


Fig. 5. (a) and (b) Comparison of the production rate of H_2O_2 (dashed line) and reaction rate of H_2O_2 (solid line). (a) The results of the 2D3PI, where there are no nanotubes in the E-matrix, i.e., H=0. (b) The results of the 3D3PI, where $H=30~\mu m$. (c) Comparison of the current generation (i) between the 2D3PI and the 3D3PI, where $d_0=50~nm$.

and sufficient supply area of oxygen can be achieved. The oxygen supply and the H_2O_2 production are thus maximized. The interfacial structures have a considerable influence on the performance. Optimizing the interfacial structures is crucial for achieving the most efficient enzymatic reaction. We will discuss the optimization in subsequent sections.

3.2. Enhanced electrochemical reaction with 3D3PI

Note that part of the H_2O_2 produced by the enzymatic reaction escapes from the E-matrix rather than participating in the subsequent electrochemical reaction. In previous studies (Zou et al., 2024), we demonstrated that the H_2O_2 escape has a very serious impact on the current generation. Therefore, maximizing H_2O_2 utilization alongside efficient H_2O_2 production is critical for enhancing the current generation. To visualize the H_2O_2 escape, we plot the production rate and the reaction rate of H_2O_2 together (Fig. 5). The schematic diagram in each sub-figure shows the structural parameters of the electrode. The difference in trend between them provides a visual representation of the H_2O_2 escape. Large differences imply more H_2O_2 loss and less efficient H_2O_2 utilization. The yellow shadow highlights the region with the maximal H_2O_2 production and utilization. In addition, the reaction rate of H_2O_2 is proportional to the current generation, and the trends of the two are completely consistent.

In the 2D3PI (Fig. 5a), the substrate is a solid nanowire array, and gas cannot be transported into the E-matrix through the nanowires. To facilitate comparison with 3D3PI, the outer diameter of the nanowire and the distance between nanowires are also denoted as d_0 and D (see the schematic diagram in Fig. 5a). Regardless of the outer diameter, as the distance increases, the production rate of H2O2 (dashed line in Fig. 5a) gradually increases and finally reaches a plateau. Based on the conclusions of our previous study (Zou et al., 2023; Zou et al., 2024), this is mainly because a wider distance can bring a larger supply area of oxygen, consequently enhancing the oxygen supply. However, previous research (Zou et al., 2024) also told us that wider distance promotes the H₂O₂ escape, thereby impeding the H₂O₂ utilization and ultimately reducing the current generation. When the distance is narrow (e.g., $D \le 1 \mu m$), increasing the distance significantly boosts the H₂O₂ production. While the distance increase also facilitates the H₂O₂ escape, the effect is not too significant. Fig. S4a shows that the escape ratio of H₂O₂ is less than 5%. At this time, the evolution trend of the reaction rate of H₂O₂ is almost consistent with the production rate of H₂O₂, and the difference between them is insignificant. Nevertheless, when the distance becomes wider (e.g., $D>10~\mu m$), the H_2O_2 escape becomes more significant, leading to a growing difference between the reaction rate and the production rate of H_2O_2 . Fig. S4a shows that the escape ratio of H_2O_2 generally exceeds 20% and can finally reach up to 86%. When the production rate of H_2O_2 reaches a peak, the reaction rate of H_2O_2 is at its lowest. These results highlight a critical defect of the 2D3PI, i.e., the inability to simultaneously maximize both H_2O_2 production and H_2O_2 utilization. In other words, a trade-off between the enhancement of enzymatic reaction and electrochemical reaction must be rigorously taken into account to maximize the electrode performance.

As shown in Fig. 5b, the results for the 3D3PI are in sharp contrast to those for the 2D3PI. It can be observed that regardless of the outer diameter of the nanotube, as the distance between two adjacent nanotubes becomes wider, the changing trends of the production rate and the reaction rate of H₂O₂ are almost identical, and the difference between the two is also negligible (the dashed line and the solid line almost coincide). It implies that the H₂O₂ escape in the 3D3PI is not significant. Fig. S4b shows that even though the distance between two adjacent nanotubes varies greatly, the escape ratio of H2O2 is generally less than 7%. This is mainly because the 3D3PI provides a larger surface area for electrochemical reaction and also changes the diffusion distance of H₂O₂, thereby improving the H₂O₂ utilization. These results indicate that the 3D3PI can ensure that enzymatic and electrochemical reactions are simultaneously optimal. In addition to significant enhancement of H₂O₂ production, efficient H₂O₂ utilization is another huge advantage of the 3D3PI compared to the 2D3PI.

Fig. 5c compares the evolution of the current generation between 2D3PI and 3D3PI when $d_o=50\,\text{nm}.$ It can be found that regardless of the distance between two adjacent substrates, the current generation of 3D3PI is always several orders of magnitude higher than that of 2D3PI. At the optimal distance (about $1\,\mu\text{m}$), the difference is as high as 32 times. This intuitively demonstrates the important role of 3D3PI in improving the current generation.

3.3. Optimized interfacial structure design for 3D3PI

While previous sections predict the existence of optimal structures for the 3D3PI, identifying these structures intuitively remains a challenging task. We systematically designed comprehensive in silico experiments to quantify the optimal ranges for each design parameter. When any one of these parameters is given, we can identify the optimal range for the remaining parameters. Notably, the penetration depth of

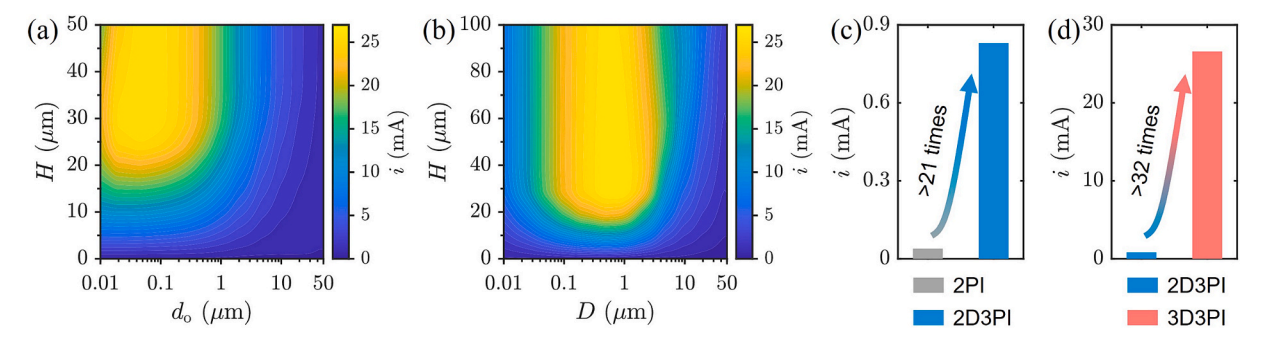


Fig. 6. Identification of optimal interfacial structures for the electrode with 3D3PI. (a) shows the effect of d_0 and H on i, where D=1 μm. (b) shows the effect of D and H on i, where $d_0=0.05$ μm. (c) Comparison of maximum current generation in electrodes with 2PI and 2D3PI. (d) Comparison of maximum current generation in electrodes with 2D3PI and 3D3PI.

the nanotube into the E-matrix (i.e., the most readily adjustable parameter in electrode fabrication) is of particular interest. Here, we focus on the design of the penetration depth and two other key parameters, as depicted in the contour plots of Fig. 6a and b. These plots enable straightforward determination of the optimal range for the remaining parameter when the value of either the outer diameter of the nanotube or the distance between two adjacent nanotubes is given. It can be seen clearly that slender (e.g., $d_{\rm o}=0.05~\mu{\rm m}$) nanotubes arranged at moderate distances (e.g., $D=1~\mu{\rm m}$) and deeply penetrated (e.g., $H=30~\mu{\rm m}$) into the E-matrix can offer maximum current generation. This quantitative information provides valuable guidance for the design of next-generation high-performance enzyme electrodes with the 3D3PI.

Fig. 6c compares the maximum current generation in the conventional 2PI and 2D3PI. Under the conditions we tested, the 2D3PI demonstrated a significant enhancement in the current generation, achieving up to a 21-fold increase compared to the 2PI. This emphasizes the advantage of three-phase interfaces over two-phase interfaces. Furthermore, Fig. 6d compares the maximum current generation in the 2D3PI and 3D3PI. The 3D3PI achieved a remarkable up to 32-fold enhancement in the current generation relative to the 2D3PI, indicating the advantage of 3D interfaces over 2D interfaces. By integrating the advantages of both three-phase interfaces and 3D interfaces in the new 3D3PI, a staggering 672-fold enhancement in current generation compared to 2PI was realized ultimately.

4. Conclusions

In this study, we developed a comprehensive mathematical model for the enzyme electrode with a 3D3PI, enabling detailed analysis of coupled transport phenomena and cascade reactions taken place in the electrode. We systematically evaluated the effect of the key structural parameters of the electrode, which include the inner diameter and the outer diameter of the nanotube, the penetration depth of the nanotube into the E-matrix, and the distance between two adjacent nanotubes, on its performance and revealed the underlying mechanisms. Moreover, we identified the optimal parameter ranges through a series of numerical experiments. The model reveals that both $\rm H_2O_2$ production and $\rm H_2O_2$ utilization determine the current generation. Our key findings are summarized below,

- 1. The 3D3PI significantly expands the interfacial area available for both oxygen supply and the electrochemical reaction compared with the 2D3PI. This leads to a substantial enhancement in both enzymatic reaction (for H_2O_2 production) and electrochemical reaction (for H_2O_2 utilization).
- 2. When enhancing H_2O_2 production (or enzymatic reaction) by regulating interfacial structures, the 2D3PI electrodes inevitably reduce H_2O_2 utilization (or electrochemical reaction), leading to a trade-off between maximizing enzymatic and electrochemical reactions. In

- contrast, our 3D3PI can simultaneously enhance both H_2O_2 production and utilization, thus maximizing cascade reactions without any trade-offs.
- 3. An optimal 3D3PI structure should be built with slender (about 0.05 μ m) hollow nanotubes arranged at moderate distances (about 1 μ m) and deeply penetrated (e.g., $H=30~\mu$ m) into the E-matrix. This configuration can not only effectively expand the area available for oxygen supply and electrochemical reaction, but also ensure a sufficient enzyme amount. This balance is essential for pushing up the kinetics limit of the enzymatic and electrochemical cascade reactions, ultimately achieving a maximal current generation.

In summary, this study offers theoretical insights into the transport phenomena in the 3D3PI enzyme electrode and presents efficient design strategies for the next-generation high-performance enzyme electrode. By resorting to mathematical modeling, the trial-and-error costs on the experiments can be significantly reduced. We are confident that experimental implementation of the 3D3PI in enzyme electrodes can be realized in the near future.

CRediT authorship contribution statement

Siyu Zou: Writing – review & editing, Writing – original draft, Visualization, Validation, Software, Methodology, Investigation, Formal analysis, Data curation. **Jie Xiao:** Writing – review & editing, Supervision, Resources, Methodology, Formal analysis, Conceptualization. **Xinjian Feng:** Writing – review & editing, Supervision, Resources, Project administration, Methodology, Funding acquisition, Formal analysis, Conceptualization.

Declaration of competing interest

The authors declare that they have no known competing financial interests or personal relationships that could have appeared to influence the work reported in this paper.

Acknowledgments

This work was supported by the National Key R&D Program of China (2019YFA0709200), the National Natural Science Foundation of China (21988102, 21978184), the Jiangsu Funding Program for Excellent Postdoctoral Talent, the Priority Academic Program Development of Jiangsu Higher Education Institutions (PAPD), and the Project of Scientific and Technologic Infrastructure of Suzhou (SZS201905). Prof. Jie Xiao acknowledges the "Jiangsu Innovation and Entrepreneurship (Shuang Chuang) Program" and the "Jiangsu Specially-Appointed Professors Program".

Appendix A. Supplementary data

Supplementary data to this article can be found online at https://doi.org/10.1016/j.ces.2025.122189.

Data availability

The numerical data from Figures 3-6 and S2-S4 are tabulated in the Supporting Information.

References

- Bard, A.J., Faulkner, L.R., White, H.S., 2022. Electrochemical methods: fundamentals and applications, 3 ed. John Wiley & Sons, New York.
- Baronas, R., Ivanauskas, F., Kulys, J., 2021. Mathematical modeling of biosensors: an introduction for chemists and mathematicians, 2 ed. Springer, Cham.
- Bartlett, P.N., Pratt, K.F.E., 1993. Modelling of processes in enzyme electrodes. Biosens. Bioelectron. 8, 451–462.
- Bird, R.B., Stewart, W.E., Lightfoot, E.N., 2006. Transport Phenomena, 2 ed. John Wiley & Sons, New York.
- Bui, J.C., Lees, E.W., Pant, L.M., Zenyuk, I.V., Bell, A.T., Weber, A.Z., 2022. Continuum Modeling of Porous Electrodes for Electrochemical Synthesis. Chem. Rev. 122, 11022–11084.
- Chen, X.-M., Xiao, J., Zhu, Y.-P., Luo, Z.-H., 2013. Intraparticle Mass and Heat transfer Modeling of Methanol to Olefins Process on SAPO-34: a Single Particle Model. Ind. Eng. Chem. Res. 52, 3693–3707.
- Clay, M., Monbouquette, H.G., 2018. A Detailed Model of Electroenzymatic Glutamate Biosensors to Aid in Sensor Optimization and in applications in Vivo. ACS Chem. Nerosci. 9, 241–251.
- Gao, M., Hazelbaker, M.S., Kong, R., Orazem, M.E., 2018. Mathematical model for the electrochemical impedance response of a continuous glucose monitor. Electrochim. Acta 275, 119–132.
- Gao, M., Orazem, M.E., 2021. The development of advanced mathematical models for continuous glucose sensors. Electrochim. Acta 382, 138226.
- Geankopolis, C.J., 1993. Transport Processes and Unit Operations, 3 ed. Prentice-Hall, Englewood.
- Goyal, A., Bairagi, P.K., Verma, N., 2020. Mathematical Modelling of a Non-enzymatic Amperometric Electrochemical Biosensor for Cholesterol. Electroanalysis 32, 1251–1262.
- Guan, F., Zhang, J., Tang, H., Chen, L., Feng, X., 2019. An enhanced enzymatic reaction using a triphase system based on superhydrophobic mesoporous nanowire arrays. Nanoscale Horiz. 4, 231–235.
- He, W.Y., Wang, C.Y., Wang, H.M., Jian, M.Q., Lu, W.D., Liang, X.P., Zhang, X., Yang, F. C., Zhang, Y.Y., 2019. Integrated textile sensor patch for real-time and multiplex sweat analysis. Sci. Adv. 5, eaax0649.

- Langer, R., 2019. Chemical and Biological Approaches to Regenerative Medicine and Tissue Engineering. Molecular Frontiers Journal 03, 122–128.
- Langer, R., Peppas, N.A., 2024. A Bright Future in Medicine for Chemical Engineering. Nat. Chem. Eng. 1, 10–12.
- Lees, E.W., Bui, J.C., Romiluyi, O., Bell, A.T., Weber, A.Z., 2024. Exploring CO reduction and crossover in membrane electrode assemblies. Nat. Chem. Eng. 1, 340–353.
- Lei, Y., Sun, R., Zhang, X., Feng, X., Jiang, L., 2016. Oxygen-Rich Enzyme Biosensor based on Superhydrophobic Electrode. Adv. Mater. 28, 1477–1481.
- Mell, L.D., Maloy, J.T., 1975. A Model for the amperometric enzyme electrode obtained through digital simulation and applied to the immobilized glucose oxidase system. Anal. Chem. 47, 299–307.
- Mi, L., Yu, J., He, F., Jiang, L., Wu, Y., Yang, L., Han, X., Li, Y., Liu, A., Wei, W., Zhang, Y., Tian, Y., Liu, S., Jiang, L., 2017. Boosting Gas involved Reactions at Nanochannel Reactor with Joint Gas–Solid–Liquid Interfaces and Controlled Wettability. J. Am. Chem. Soc. 139, 10441–10446.
- Parker, J.W., Schwartz, C.S., 1987. Modeling the kinetics of immobilized glucose oxidase. Biotechnol. Bioeng. 30, 724–735.
- Parker, R.S., Doyle, F.J., Peppas, N.A., 1999. A model-based algorithm for blood glucose control in Type I diabetic patients. IEEE Trans. Biomed. Eng. 46, 148–157.
- Peppas, N.A., Langer, R., 2004. Origins and development of biomedical engineering within chemical engineering. AIChE J 50, 536–546.
- Peppas, N.A., Narasimhan, B., 2014. Mathematical models in drug delivery: how modeling has shaped the way we design new drug delivery systems. J. Control. Release 190, 75–81.
- Poling, B.E., Prausnitz, J.M., O'connell, J.P., 2001. The properties of gases and liquids, 5 ed. Mcgraw-hill, New York.
- Sander, R., 2015. Compilation of Henry's law constants (version 4.0) for water as solvent. Atmos. Chem. Phys. 15, 4399–4981.
- Song, Z., Xu, C., Sheng, X., Feng, X., Jiang, L., 2018. Utilization of Peroxide Reduction Reaction at Air–Liquid–Solid Joint Interfaces for Reliable Sensing System Construction. Adv. Mater. 30, 1701473.
- Tao, Z., Raffel, R.A., Souid, A.-K., Goodisman, J., 2009. Kinetic studies on enzymecatalyzed reactions: oxidation of glucose, decomposition of hydrogen peroxide and their combination. Biophys. J. 96, 2977–2988.
- Teymourian, H., Barfidokht, A., Wang, J., 2020. Electrochemical glucose sensors in diabetes management: an updated review (2010-2020). Chem. Soc. Rev. 49, 7671–7709.
- Wang, H., Zhang, J., Wang, D., Wang, Z., Chen, Y., Feng, X., 2021. Flexible triphase enzyme electrode based on hydrophobic porous PVDF membrane for highperformance bioassays. Biosens. Bioelectron. 183, 113201.
- Yang, Y.R., Song, Y., Bo, X.J., Min, J.H., Pak, O.S., Zhu, L.L., Wang, M.Q., Tu, J.B., Kogan, A., Zhang, H.X., Hsiai, T.K., Li, Z.P., Gao, W., 2020. A laser-engraved wearable sensor for sensitive detection of uric acid and tyrosine in sweat. Nat. Biotechnol. 38. 217–224.
- Zou, S., Wang, D., Xiao, J., Feng, X., 2023. Mathematical Model for a Three-phase Enzymatic Reaction System. Ind. Eng. Chem. Res. 62, 4337–4343.
- Zou, S., Xiao, J., Feng, X., 2024. Modeling enzymatic and electrochemical cascade reactions at the three-phase interface enzyme electrode. AIChE J e18420.